5-16-2007

Seasonal Variations of the Vertical Fluxes of Heat and Horizontal Momentum in the Mesopause Region at Starfire Optical Range, New Mexico

Chester S. Gardner

Alan Z. Liu

Embry Riddle Aeronautical University - Daytona Beach, liuz2@erau.edu

Seasonal variations of the vertical fluxes of heat and horizontal momentum in the mesopause region at Starfire Optical Range, New Mexico

Chester S. Gardner[1] and Alan Z. Liu[1]

Received 4 May 2005; revised 2 November 2006; accepted 21 December 2006; published 10 May 2007.

[1] Lidar observations of wind and temperature profiles between 85 and 100 km, conducted at the Starfire Optical Range (SOR), New Mexico, are used to characterize the seasonal variations of the vertical fluxes of heat and horizontal momentum and their relationships to gravity wave activity in this region. The wind and temperature variances exhibit strong 6-month oscillations with maxima during the summer and winter that are about 3 times larger than the spring and fall minima. The vertical heat flux also exhibits strong 6-month oscillations with maximum downward flux during winter and summer. The downward heat flux peaks near 88 km where it exceeds -3 K m s^{-1} in mid-winter and is nearly zero during the spring and fall equinoxes. The heat flux is significantly different from zero only when the local instability probability exceeds 8%, i.e., the annual mean for the mesopause region. The momentum fluxes also exhibit strong seasonal variations, which are related to the horizontal winds. Two-thirds of the time the horizontal momentum flux is directed against the mean wind field.

Citation: Gardner, C. S., and A. Z. Liu (2007), Seasonal variations of the vertical fluxes of heat and horizontal momentum in the mesopause region at Starfire Optical Range, New Mexico, *J. Geophys. Res.*, *112*, D09113, doi:10.1029/2005JD006179.

1. Introduction

[2] Atmospheric gravity waves (AGWs) strongly influence middle-atmosphere circulation and structure by vertically transporting horizontal momentum, heat, and constituents when they experience dissipation [*Matsuno*, 1982; *Holton*, 1983; *Garcia and Solomon*, 1985; *Hamilton*, 1996; *Alexander and Holton*, 1997; *Walterscheid*, 2001]. Dissipation is caused by several mechanisms including convective and dynamic instabilities, nonlinear wave-wave and wave-mean flow interactions, and critical layer filtering [*Hodges*, 1969; *Hines*, 1970; *Lindzen*, 1981]. Gravity wave drag plays a significant role in establishing the zonal mean wind profile in the middle atmosphere [*Fritts and Luo*, 1995; *Luo et al.*, 1995; *Hamilton*, 1996; *Fritts and Alexander*, 2003]. In addition, dissipating gravity waves typically transport heat downward, which can result in substantial cooling of the middle atmosphere as heat is transported to lower altitudes [*Walterscheid*, 1981; *Weinstock*, 1983; *Gardner and Yang*, 1998].

[3] Momentum and heat transport is characterized by the vertical fluxes of these parameters. Vertical fluxes are second-order statistics of the gravity wavefield, which quantify the cross-correlation between the wave-induced vertical wind perturbations and the associated horizontal wind and temperature fluctuations. These statistics are difficult to measure because they are typically small in quantities, while the wind and temperature variances are large. To ensure that observations include the effects of the important high-frequency (HF), small-vertical-scale waves, the atmospheric parameters must be measured with good accuracy at high resolution ($\sim$ 2 min and $\sim$ 1 km). Furthermore, extremely long averaging times ($\sim$ day) are required to obtain statistically significant flux estimates [*Gardner and Yang*, 1998; *Kudeki and Franke*, 1998; *Thorsen et al.*, 2000]. Because nondissipating gravity waves have zero heat flux, measurement of the heat flux is especially challenging but can provide a direct measure of gravity wave dissipation [*Gardner et al.*, 2002].

[4] Na wind/temperature lidar is capable of making the momentum and heat flux measurements when the instrument is coupled to a steerable telescope. From 1998 to 2000, the University of Illinois Na lidar was deployed at Starfire Optical Range, New Mexico (SOR, 35.0°N, 106.5°W) and 370 hours of horizontal and vertical wind, temperature, and Na density measurements were obtained using the facility's 3.5-m-diameter astronomical telescope. *Liu and Gardner* [2004, 2005] used this data set to determine the annual mean heat and Na flux profiles in the mesopause region at the site. In this paper, we use the same data set to derive and analyze the seasonal variations of the vertical fluxes of heat and horizontal momentum. The primary objective is to quantify the annual mean fluxes and their 12- and 6-month oscillations between 85 and 100 km. A secondary objective is to determine the relationships among the 12- and 6-month flux variations and the corresponding variations in gravity wave activity, the background wind and temperature structure, and the stability conditions in the mesopause region at this site.

[1]Department of Electrical and Computer Engineering, University of Illinois Urbana, Illinois, USA.

0148-0227/07/2005JD006179$09.00

Table 1. Statistics of the Wind and Temperature Observations[a]

	January	February	March	April	May	June	July	August	September	October	November	December	Annual Total	Monthly Average
Observation Nights	5	2	3	6	6	4	–	3	6	5	4	5	49	4.5
Observation Hours	45.9	16.6	22.3	41.0	40.9	26.7	–	16.0	37.5	42.4	27.7	52.6	369.7	33.6
$\overline{(u')^2}$, m^2 s^{-2}	389	318	247	230	266	299	–	234	206	244	330	397	–	287
$\overline{(v')^2}$, m^2 s^{-2}	597	457	247	155	250	419	–	391	242	211	353	542	–	363
$\overline{(w')^2}$, m^2 s^{-2}	3.2	2.6	1.6	1.8	3.7	6.2	–	6.1	3.7	1.9	1.8	2.7	–	3.5
$\overline{(T')^2}$, K^2	92.0	82.4	58.3	42.0	46.9	65.0	–	66.8	47.7	39.2	52.7	77.8	–	62.2

[a]Variances of wind and temperature fluctuations represent averages between 85 and 100 km.

[5] Seasonal variations are more difficult to measure than the annual means because shorter data averaging times are required. By using the horizontal and vertical wind and temperature profiles measured by the lidar at SOR, we derived the gravity wave perturbations and calculated the variances and covariances among these quantities on a monthly basis. The monthly mean profile data were then fitted to a harmonic model that included the 12- and 6-month oscillations. The uncertainties in the measured and fitted parameters are carefully analyzed to assess the robustness of the inferred seasonal variations.

2. Observations

[6] The lidar observations analyzed in this paper were conducted at the Starfire Optical Range (SOR) located on the Kirtland Air Force Base (AFB; 35°N, 106.5°W), near Albuquerque, NM. The facility is operated by the Air Force Research Laboratory, Directed Energy Directorate and includes a 3.5-m-diameter astronomical telescope. The University of Illinois Na wind/temperature lidar was coupled to this telescope through the coude path so that the beam could be pointed in any direction. In the normal operation mode, the lidar was pointed at zenith (Z) and 10° off-zenith to the north (N), south (S), east (E), and west (W) in the following sequence: ZNEZSW. At each position, temperature and line-of-sight (LOS) wind profiles were obtained at 500-m vertical and 90-s temporal resolution. These profiles include the perturbations associated with gravity waves having vertical wavelengths longer than 1 km and observed periods longer than 3 min. The data include the effects of the important short-vertical-scale, high-frequency gravity waves that are most susceptible to dissipation and that make the largest contributions to the heat and momentum fluxes.

[7] The root mean square (RMS) LOS wind and temperature errors average about 1.0 m s^{-1} and 1.3 K between 85 and 100 km, respectively. The 1-mrad pointing accuracy of the lidar was limited by the divergence of the laser beam and the field-of-view of the detector. At this pointing accuracy, the horizontal wind contamination in the vertical wind measurement was generally less than 0.1 m s^{-1}, depending on horizontal wind speed, which is much less than measurement errors associated with photon noise. Details of the experimental setup, data processing, and measurement validation can be found in the works of *Gardner et al.* [2002], *Liu et al.* [2002], *Liu and Gardner* [2004], *Franke et al.* [2005], and *Chu et al.* [2005]. Methods used for extracting the gravity wave perturbations from the measured wind and temperature profiles and for computing wave variances, momentum fluxes, and heat fluxes are described in the Appendix.

[8] Measurements were made only at night, on a campaign basis from June 1998 to November 2000 during the 2-week periods surrounding new moon. Data were available for every calendar month except July. Observations typically commenced at sunset and continued until sunrise. For this study we employ 370 hours of data that were collected throughout the 30-month period. The number of observation hours varies from 16 in August to over 50 in December. On average there are 33 hours or 4.5 nights of observation each month. Key statistics for these observations, including numbers of observational nights and hours and variances of three wind components and temperature, are summarized for each month in Table 1. The data coverage during the night for each hour is shown in Figure 1. Every month

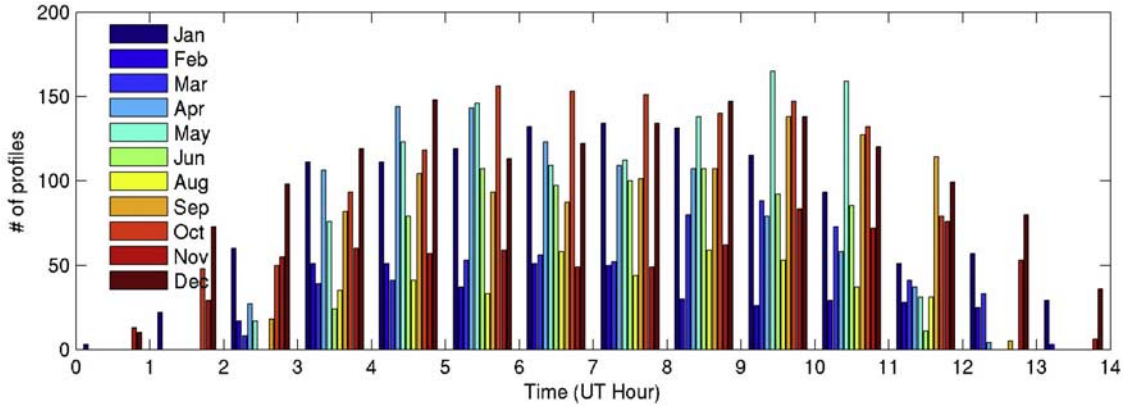

Figure 1. Distribution of number of profiles at each UT hour for each calendar month.

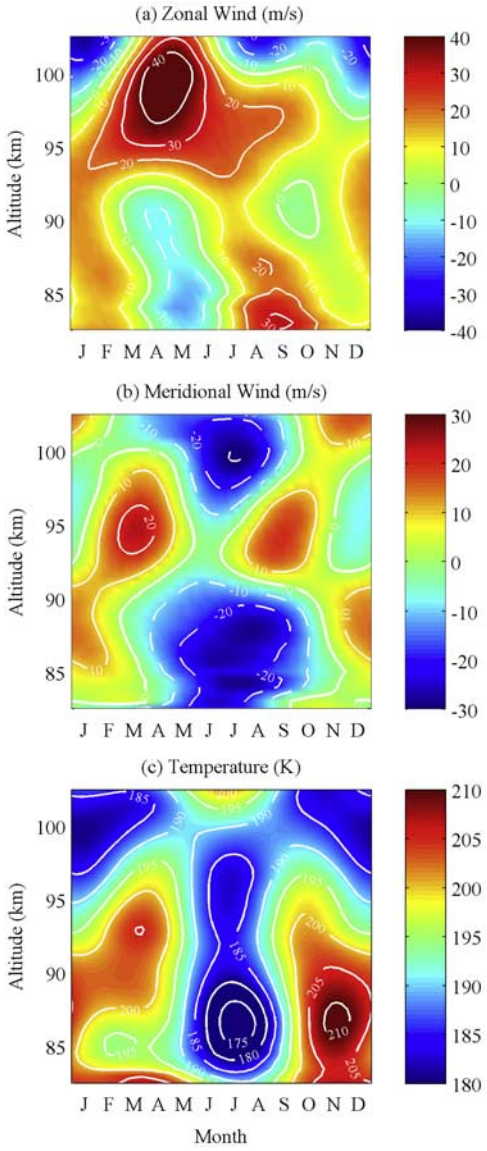

Figure 2. Seasonal variations of nighttime (a) zonal wind, (b) meridional wind, and (c) temperature in the mesopause region at Starfire Optical Range, NM.

except July, there are data available between 3 and 12 UT (8 p.m. to 5 a.m. local time).

3. Seasonal Variations of the Wind and Temperature

[9] Because momentum and heat fluxes are influenced by the strength and directionality of the gravity wavefield, by the stability of the atmosphere, and by the strength and direction of the horizontal wind field, we first examine the seasonal variations in the mean structure of the atmosphere and their relationships to atmospheric stability. The mean wind and temperature were derived by first averaging the data in local time at a 30-min resolution to construct a composite night for each month. The composite nights were then averaged over the 10-hour period centered about local midnight to derive the monthly mean profiles. This method eliminates potential biases associated with unequal observation hours for different times of the night. Because of strong tidal variations in the mesopause region, equal weighting at every hour of the night is important to avoid sampling biases, which can affect the mean values. Due to the small number of observations nights per month, the monthly averaged quantities are still susceptible to daily variations. To minimize the residual effects of daily variations and highlight the seasonal variation, the monthly mean quantities were fitted to a model that includes the annual mean plus 12- and 6-month oscillations. This fitted seasonal variation of horizontal wind and temperature is shown in Figure 2 at 500-m and 1-week intervals. The seasonal variations in these parameters are generally consistent with previous observations at northern midlatitudes and with our knowledge of the general circulation of the mesosphere and lower thermosphere.

[10] The zonal wind is directed eastward throughout most of the year. The strongest velocities occur above 95 km during the spring equinox when they exceed +40 m s^{-1}. Below 95 km during this period, there is a weak westward jet with velocities that approach −10 to −20 m s^{-1}. Elsewhere, the velocities are less than about +20 m s^{-1}. The meridional wind is directed toward the wintertime pole throughout the mesopause region, which is consistent with the diabatic circulation system. The maximum velocities are about 10–20 m s^{-1} northward in winter and 20–30 m s^{-1} southward in summer.

[11] The mean temperature structure is closely related to the meridional wind. The coldest temperatures occur near 86 km in July and August. These cold temperatures are the result of adiabatic cooling associated with the summertime upwelling over the northern hemisphere and the subsequent southward flow and then downwelling over the south polar cap. The reverse happens in winter. In general, relatively warm winter temperatures are associated with northward meridional flow while cold summer temperatures are associated with southward flow in northern latitudes.

[12] The convective or static stability of the atmosphere is characterized by the square of the buoyancy frequency N defined as

$$N^2 = \frac{g}{T}\left(\frac{\partial T}{\partial z} + \frac{g}{C_p}\right), \tag{1}$$

where g is the gravitational acceleration, equal to 9.5 m s^{-2} in the mesopause region; T is the atmospheric temperature; and C_p is the specific heat at constant pressure, equal to 1004 J K^{-1} kg^{-1}. When N^2 is positive, the atmosphere is statically stable. When N^2 is negative, that is, when the atmospheric lapse rate $-\partial T/\partial z$ is larger than the adiabatic lapse rate $g/C_p \approx 9.5$ K km^{-1}, the atmosphere is unstable.

[13] Shear or dynamic instability is induced by large vertical shears of the horizontal wind in combination with low static stability. Dynamic stability is characterized by the Richardson number Ri which is defined as

$$Ri = \frac{N^2}{(\partial u/\partial z)^2 + (\partial v/\partial z)^2} = \frac{N^2}{S^2}, \tag{2}$$

where S is the total vertical shear of horizontal wind, equal to $[(\partial u/\partial z)^2 + (\partial v/\partial z)^2]^{1/2}$, and u and v are the zonal and

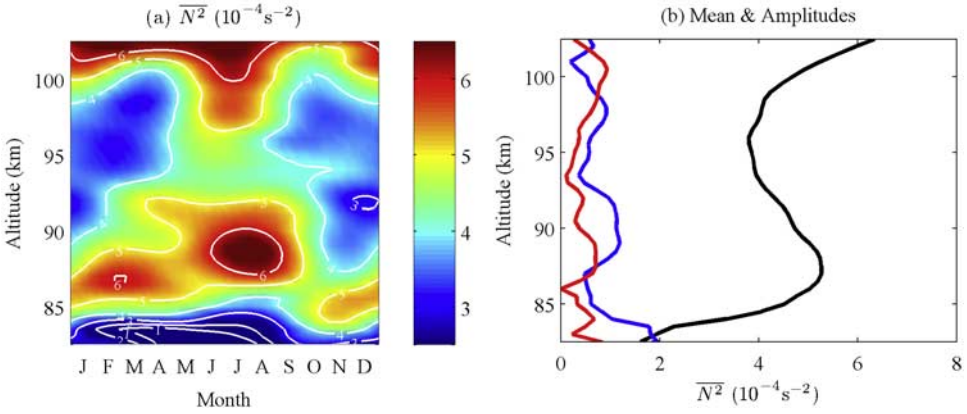

Figure 3. (a) Seasonal variations of squared buoyancy frequency $\overline{N^2}$ plotted versus altitude and month and (b) annual mean profile (black) and 12-month (blue) and 6-month (red) amplitudes.

meridional wind velocities, respectively. Generally, the atmosphere is considered to be dynamically unstable when $0 < Ri < 1/4$. Dynamic instability occurs when there is a strong wind shear and/or small static stability. *Hodges* [1967] pointed out that for the mean atmosphere without gravity waves, it is unlikely for the condition of dynamic instability to be satisfied. But in the presence of gravity waves and tides, large vertical shears of the temperature and horizontal wind can be generated, which often results in thin layers of instability [*Fritts and Rastogi*, 1985; *Zhao et al.*, 2003].

[14] To characterize the static stability of the mean atmosphere, the monthly average values of the square of the buoyancy frequency $\overline{N^2}$ were computed using the average monthly temperature and then fitted to a model that includes the mean plus 12- and 6-month oscillations. The results are plotted in contour format in Figure 3a. The annual mean profile and the amplitudes of the 12- and 6-month oscillations are plotted versus altitude in Figure 3b. This method of computing $\overline{N^2}$ overestimates static stability because most of the gravity wave and semidiurnal tidal perturbations have been eliminated by the data averaging that is employed to derive the monthly mean temperature profiles. However, the resulting $\overline{N^2}$ data are excellent indicators of the regions of low stability where wave dissipation is expected to be greatest [*Gardner et al.*, 2002]. For the SOR data, the atmosphere is statically stable on average throughout the mesopause region. The region of lowest average stability, where $\overline{N^2}$ exhibits the smallest values, lies between 82.5 and 85 km (see Figure 3). The region of greatest average stability lies between 97.5 and 102.5 km, where the temperature increases with increasing altitude throughout the year.

[15] The wind, temperature, and $\overline{N^2}$ profiles all exhibit strong seasonal variations. These variations contribute to variation in wave filtering and dissipation due to instabilities, which lead to seasonal variation of gravity wave activity and their fluxes in this region.

4. Seasonal Variations of the Gravity Wave Activity

[16] Variations in gravity wave activity can affect atmospheric stability as well as the momentum and heat fluxes. In this section, we examine the variances of temperature and wind, which are indicators of wave activity. These variances were derived using the same perturbation data that were used to compute the flux profiles (see Appendix). The monthly mean variance profiles have a vertical resolution of 2.5 km and include the effects of all waves with vertical wavelengths greater than 1 km and less than about 30 km and periods greater than 3 min and less than about 14 hours. The 12- and 6-month variance oscillations were characterized by employing the same fitting procedure used to determine the seasonal variations of the wind and temperature profiles.

[17] The perturbation variances of the three wind components are shown in Figure 4. The temperature variance is plotted in Figure 5. The most striking feature is the pronounced minima throughout the 85- to 100-km height range during the equinox periods for all parameters. Clearly, the periods of weakest gravity wave activity occur during the equinoxes while the strongest occur during mid-winter and mid-summer.

[18] The annual mean zonal and meridional wind variances are comparable and they generally grow with increasing altitude from about 225 m^2 s^{-2} near 85 km to about 400 m^2 s^{-2} near 100 km (Figures 4b and 4d). For the zonal wind variance, the amplitudes of the 12- and 6-month oscillations are relatively small compared with the annual mean. In contrast, the meridional wind variance exhibits especially strong 6-month oscillations with amplitudes that reach 300 m^2 s^{-2} near 97.5 km where the annual mean is about 400 m^2 s^{-2}. As a consequence of these oscillations, the total horizontal wind variance (Figures 4e and 4f) changes by more than a factor of 3 during the year with maximum values in mid-winter and mid-summer and minimum values during the spring and fall equinoxes.

[19] The mean vertical wind variance is approximately 4 m^2 s^{-2} between 85 and 92.5 km, then decreases rapidly to 3 m^2 s^{-2} at 95 km where it remains constant throughout the remainder of the height range (Figures 4g and 4h). The vertical wind variance exhibits strong 12-month oscillations with amplitudes that reach almost 3 m^2 s^{-2} near 92.5 km where the annual mean is about 4 m^2 s^{-2}. The largest variances occur below 95 km in mid-summer where they exceed 7 m^2 s^{-2} and the minimum values occur at the equinoxes where they are less than 2 m^2 s^{-2}.

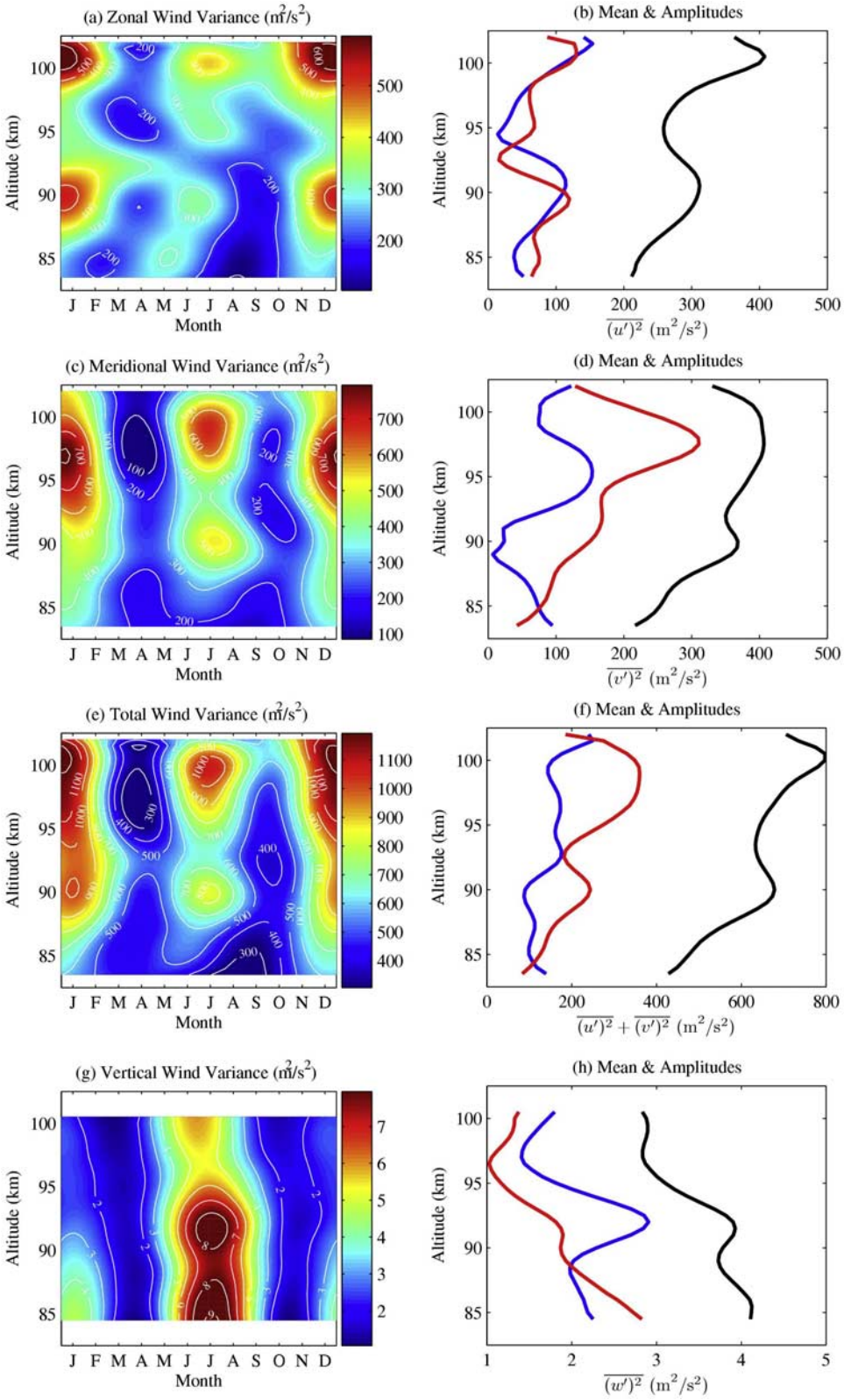

Figure 4. Similar to Figure 3, except for the wind variances: ((a) and (b)) zonal wind variance, ((c) and (d)) meridional wind variance, ((e) and (f)) total horizontal wind variance, ((g) and (h)) vertical wind variance.

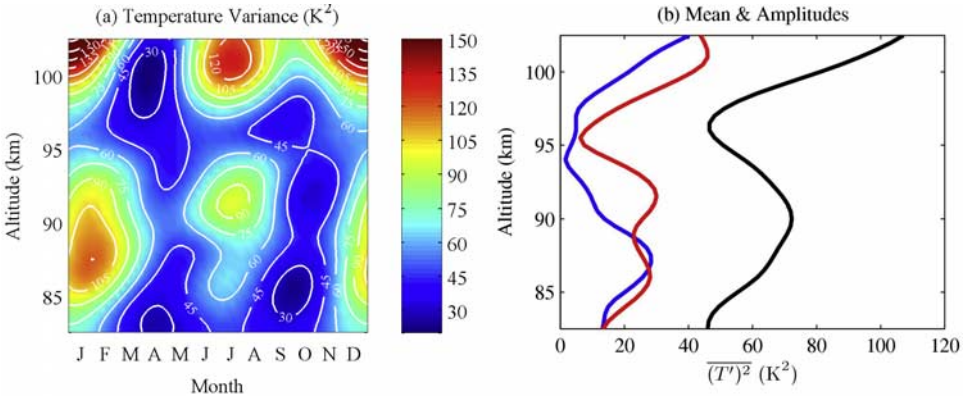

Figure 5. Similar to Figure 3 except for temperature variance.

[20] Radar techniques have also been used to measure wind variances. *Tsuda et al.* [1990] measured the wind variance in the region between 60 and 85 km at 35°N using the middle and upper atmosphere (MU) radar and also found strong semiannual variation with minima at the equinoxes. They reported that the zonal wind variance had a maximum of about 200 m^2 s^{-2} in summer and 50 m^2 s^{-2} at the equinoxes for wave periods between 0.5 and 2 hours. *Vincent and Fritts* [1987] also detected the semi-annual oscillation in wind variance using the HF radar at Adelaide (35°S), with maxima of 300–350 m^2 s^{-2} during the solstices and minima of 200–250 m^2 s^{-2} at the equinoxes at 86-km altitude for wave periods between 1 and 24 hours. At a higher latitude, *Meek et al.* [1985] detected semi-annual variations in zonal wind component for periods less than 1 hour, with 140 m^2 s^{-2} in summer and winter and 100 m^2 s^{-2} at the equinoxes. The wave variances measured by our lidar correspond to higher altitudes and include a broader spectrum of waves with period from 3 min to 14 hours. As expected, the lidar-derived horizontal wind variances are generally larger than those measured by radars at lower altitudes and a more limited range of wave periods. However, the strong semiannual variation is consistent with radar measurements at midlatitude. The vertical wind variance measured at SOR is similar to that measured by Tsuda et al., who showed a maximum vertical wind variance of about 8 m^2 s^{-2} in July, minima of 2 m^2 s^{-2} during the equinoxes, and 4 m^2 s^{-2} in winter.

[21] The temperature variance exhibits strong 12- and 6-month oscillations with maxima near the solstices and minima during the spring and fall equinoxes (Figures 5a and 5b). The annual mean profile increases from about 45 K^2 at 82.5 km to a local maximum of about 70 K^2 near 90 km. The temperature variance then decreases reaching a local minimum of about 45 K^2 at 96 km. It then increases monotonically throughout the remainder of the height range reaching a maximum value of 110 K^2 at 102.5 km. This vertical structure appears to be related to enhanced wave dissipation below 85 km where N^2 is low and low dissipation above 96 km where N^2 is large [*Gardner et al.*, 2002].

5. Vertical Heat Flux

[22] Dissipating gravity waves transport heat as they propagate through a region. The vertical heat flux ($\overline{w'T'}$, overbar denotes sample averaging) is defined as the expected value of the product of the vertical wind (w') and temperature (T') perturbations. In the absence of wave dissipation, the wave-induced perturbations in temperature are proportional to vertical displacement so that w' and T' are orthogonal and the vertical heat flux is zero. Wave dissipation mechanisms such as convective and shear instabilities, alter the phase relationships between w' and T', thus giving rise to a net vertical heat transport and a nonzero value for the heat flux. The vertical heat flux profile is an excellent measure of wave dissipation. Dissipating waves typically transport heat downward, which can result in substantial cooling as heat is transported to lower altitudes [*Walterscheid*, 1981; *Weinstock*, 1983].

[23] Monthly mean profiles of the vertical fluxes of heat and horizontal momentum were computed from the lidar data according to the procedures described in the Appendix. The dominant seasonal variations were determined by fitting the measured monthly mean fluxes to a model that includes the annual mean plus 12- and 6-month oscillations. To illustrate the seasonal variations, the heat flux regression model is plotted in contour format in Figure 6. The dominant feature is the large downward flux below 92 km in both summer and winter. The maximum downward flux

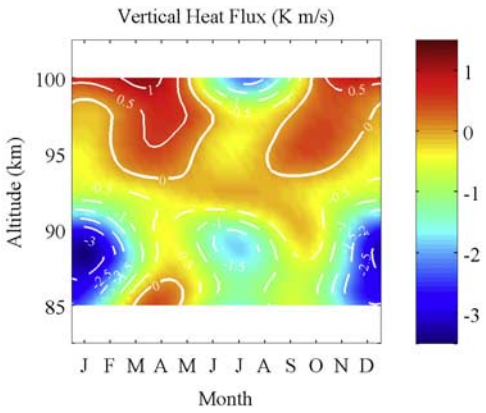

Figure 6. Seasonal variation of the measured vertical heat flux. The harmonic model uncertainties, which vary with altitude, average ±0.34 K m s^{-1} and are tabulated in Table 2. Note that the color coding is not symmetric with respect to zero.

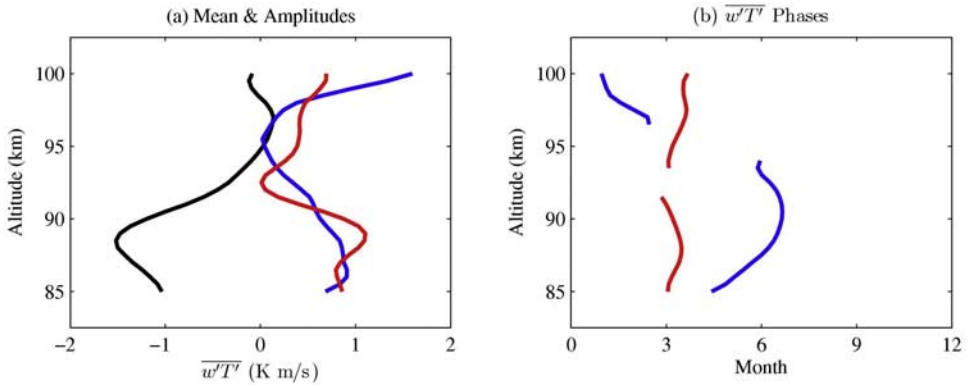

Figure 7. Harmonic fit parameters of the vertical heat flux plotted versus altitude: (a) annual mean $\overline{w'T'}$ profile (black), 12-month (blue) and 6-month (red) amplitudes, (b) 12-month (blue) and 6-month (red) $\overline{w'T'}$ phases. The measurement uncertainties for these parameters are tabulated versus altitude in Table 2.

exceeds -3 K m s^{-1} in winter and -1.5 K m s^{-1} in summer at 88 km. During the spring and fall equinoxes the heat flux is near zero below 92 km. Above 92 km, the heat flux is slightly positive throughout the year, except in summer above 97 km, where there is a large downward flux that exceeds -2 K m s^{-1}.

[24] The fitted flux parameters are plotted versus altitude in Figure 7 and their values are tabulated for every 2.5 km between 85 and 100 km in Tables 2 and 3. The errors in the fitted parameters were calculated using the standard regression formulas and the errors in the measured monthly flux profiles given by (A5). The annual mean heat flux profile exhibits a prominent maximum near 88 km of about -1.6 K m s^{-1} and is approximately zero above 95 km (Figure 7a). The seasonal variations are dominated by both 12- and 6-month oscillations throughout the mesopause region. The 6-month amplitude profile has a prominent maximum of about 1.1 K m s^{-1}, also at 88 km. This oscillation is quite apparent in the heat flux contour plot presented in Figure 6.

[25] Because nonzero downward heat fluxes are produced by dissipating gravity waves, the largest heat flux values should be coincident with those atmospheric regions that exhibit the smallest values of mean static stability ($\overline{N^2}$) and the highest probabilities of static and dynamic instabilities. Indeed, this appears to be the case for the SOR data. The annual mean downward heat flux is maximum near 88 km (Figure 7a), just above the region between 82.5 and 85 km where the annual mean $\overline{N^2}$ is smallest (Figure 3b). The mean heat flux is approximately zero above 95 km where the mean $\overline{N^2}$ is not only largest but also increases with increasing altitude. However, the strength of the gravity wave activity also plays a key role in determining the regions of greatest wave dissipation. This is illustrated by the similarities in the measured heat flux and temperature variance contours that are plotted in Figures 5a and 4a, respectively. The regions and times of maximum downward heat flux generally correspond to the regions of maximum temperature variance.

[26] The key parameter, most closely associated with wave activity, dissipation, and the heat flux, is the temperature lapse rate variance $(\partial T'/\partial z)^2$. The first law of thermodynamics

$$\frac{\partial T'}{\partial t} + \Gamma w' = D\frac{\partial^2 T'}{\partial z^2} \tag{3}$$

can be used to relate the heat flux directly to the variance of the temperature lapse rate [e.g. *Gardner*, 1994],

$$\overline{w'T'} = -\frac{D}{\Gamma}\overline{\left(\frac{\partial T'}{\partial z}\right)^2}, \tag{4}$$

where Γ is the adiabatic lapse rate for dry air. In equation (3), the change in thermal energy associated with wave dissipation is modeled as a diffusion process, where D is the effective vertical thermal diffusivity. In the absence of wave dissipation $D = 0$, the temperature perturbations are proportional to the vertical displacement perturbations (see (3)), and the heat flux is zero.

[27] The seasonal variations of the lapse rate variance were computed from the temperature perturbation profiles and the results are plotted in contour format in Figure 8a. The harmonic fit parameters are plotted in Figure 8b. The data are generally consistent with the theoretical relationship given by (4). The lapse rate variance is largest in the same regions and at the same times of the year that the heat flux has its largest downward values. In particular, the large values of downward heat flux above 97.5 km in mid-

Table 2. Measured Heat Flux Parameters

Altitude, km	Annual Mean, K m s^{-1}	12-Month Amplitude, K m s^{-1}	12-Month Phase, month	6-Month Amplitude, K m s^{-1}	6-Month Phase, month	Model Uncertainty, K m s^{-1}
100.0	−0.1 ± 0.16	1.5 ± 0.23	1.0 ± 0.3	0.7 ± 0.23	3.8 ± 0.3	±0.36
97.5	0.1 ± 0.13	0.2 ± 0.18	2.2 ± 1.7	0.4 ± 0.18	3.8 ± 0.4	±0.29
95.0	0.0 ± 0.13	0.0 ± 0.18		0.4 ± 0.18	3.2 ± 0.4	±0.29
92.5	−0.3 ± 0.16	0.3 ± 0.23	6.3 ± 1.5	0.0 ± 0.23		±0.36
90.0	−1.2 ± 0.17	0.6 ± 0.24	6.7 ± 0.8	0.9 ± 0.24	3.2 ± 0.3	±0.38
87.5	−1.4 ± 0.16	0.9 ± 0.23	6.0 ± 0.5	0.9 ± 0.23	3.5 ± 0.2	±0.36
85.0	−1.0 ± 0.14	0.7 ± 0.20	4.5 ± 0.5	0.9 ± 0.20	3.0 ± 0.2	±0.31

Table 3. Measured Zonal Momentum Flux Parameters

Altitude, km	Annual Mean, $m^2\ s^{-2}$	12-Month Amplitude, $m^2\ s^{-2}$	12-Month Phase, month	6-Month Amplitude, $m^2\ s^{-2}$	6-Month Phase, month	Model Uncertainty, $m^2\ s^{-2}$
100.0	−2.7 ± 0.78	2.6 ± 1.1	6.6 ± 0.8	2.3 ± 1.1	3.4 ± 0.5	±1.7
97.5	0.7 ± 0.56	3.1 ± 0.79	4.8 ± 0.5	3.8 ± 0.79	5.2 ± 0.2	±1.3
95.0	−0.7 ± 0.53	1.9 ± 0.75	4.1 ± 0.8	1.9 ± 0.75	4.7 ± 0.4	±1.2
92.5	−1.5 ± 0.58	2.5 ± 0.82	6.2 ± 0.6	0.6 ± 0.82	2.4 ± 1.3	±1.3
90.0	−1.0 ± 0.61	2.3 ± 0.86	6.1 ± 0.7	2.7 ± 0.86	1.7 ± 0.3	±1.4
87.5	−2.0 ± 0.58	1.5 ± 0.82	3.2 ± 1.0	2.8 ± 0.82	4.0 ± 0.3	±1.3
85.0	−1.1 ± 0.46	1.6 ± 0.59	5.4 ± 0.7	1.2 ± 0.59	4.1 ± 0.5	±1.0

summer appear to be related to especially large lapse rate variances during this same period and altitude range.

[28] Because the temperature and N^2 perturbations induced by gravity waves are Gaussian distributed random processes, the probability of convective instability can be expressed as a simple function of the complementary error function [*Zhao et al.*, 2003],

$$P(N^2 < 0) = \frac{1}{2}\mathrm{erfc}\left[\overline{N^2}\Big/\sqrt{2\mathrm{var}(N^2)}\right], \tag{5}$$

where

$$\mathrm{var}(N^2) \approx \left(\frac{g}{\overline{T}}\right)^2 \overline{\left(\frac{\partial T'}{\partial z}\right)^2}. \tag{6}$$

The measured values of $\overline{N^2}$ and $\overline{(\partial T'/\partial z)^2}$ were used to predict the probability of convective instability according to (5) and (6) and the results are plotted in contour format in Figure 9a. The harmonic fit parameters are plotted in Figure 9b. The regions with the largest values of heat flux occur at the same months as, but 3–4 km lower than, the regions with the largest probabilities of convective instability.

[29] *Zhao et al.* [2003] also derived an expression for probability of dynamic instability,

$$P(0 < Ri < 1/4) = \frac{1}{2}\ exp\left[-\frac{4\overline{N^2}}{\overline{S^2}} + \left(\frac{4\mathrm{std}(N^2)}{\sqrt{2}\overline{S^2}}\right)^2\right] \cdot \mathrm{erfc}\left(\frac{4\mathrm{std}(N^2)}{\sqrt{2}\overline{S^2}} - \frac{\overline{N^2}}{\sqrt{2}\mathrm{std}(N^2)}\right). \tag{7}$$

This formula is valid under the special conditions where the vertical shear of the mean wind field is negligible (i.e., $\overline{S^2} \approx (S')^2$) and that the zonal and meridional perturbation shear variances are equal. These conditions hold approximately for the SOR data set and so (7) can be used to identify those

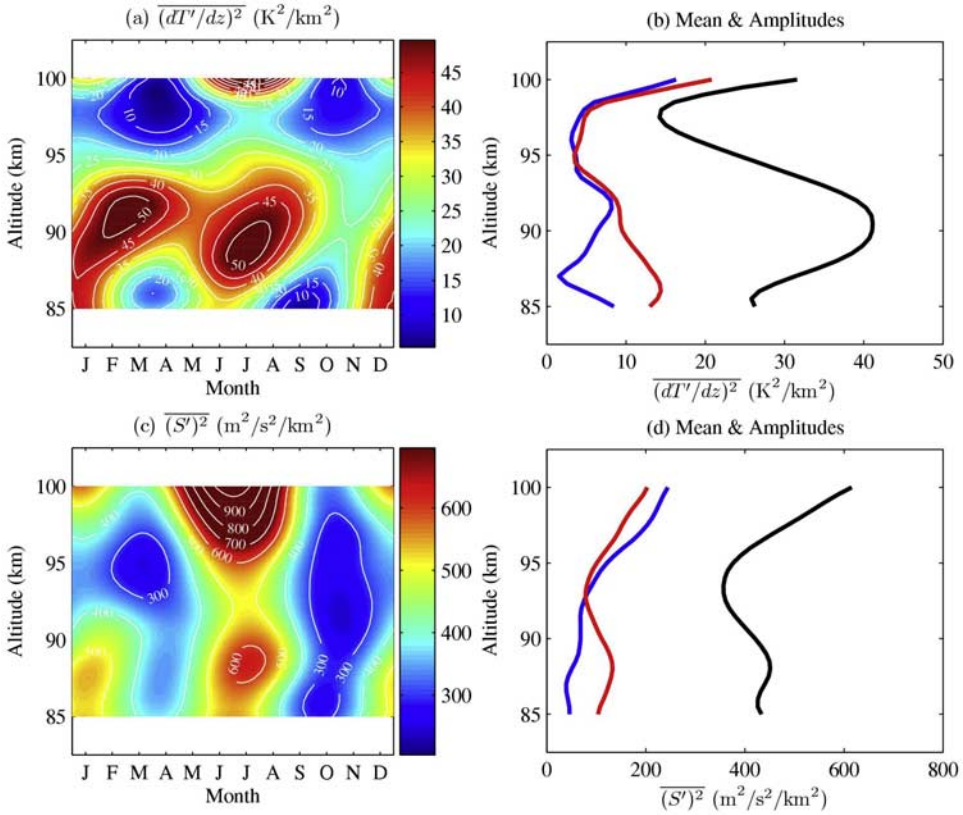

Figure 8. Similar to Figure 3 except for the measured ((a) and (b)) temperature lapse rate variance $(\partial T'/\partial z)^2$ and ((c) and (d)) wind shear variance $\overline{S'^2}$.

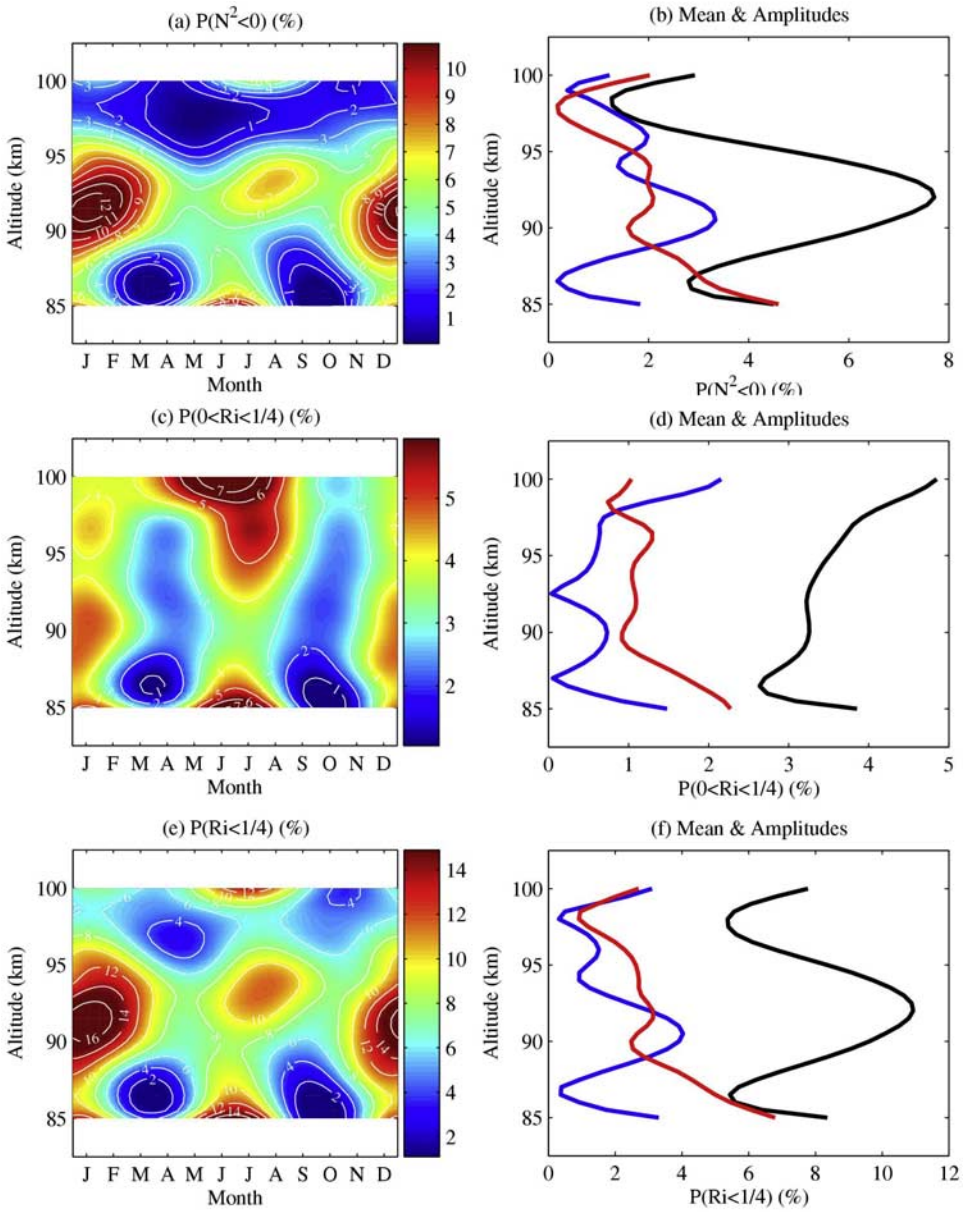

Figure 9. Similar to Figure 3 except for the probabilities of ((a) and (b)) static instability $P(N^2 < 0)$, ((c) and (d)) dynamic instability $P(0 < Ri < 1/4)$, and ((e) and (f)) total instability $P(Ri < 1/4)$.

regions where shear instabilities are likely to result in significant wave dissipation. The total shear variance $(S')^2$ was computed from the zonal and meridional wind perturbation data and the results are plotted in contour format in Figure 8c. The harmonic fit parameters are plotted in Figure 8d. The regions of local maxima of shear variance correspond closely with the regions of local maxima of downward heat flux, both below 90 km and above 95 km in summer and below 90 km in winter, which suggests that dynamic instabilities play an important role in the wave dissipation in the mesopause region. The probability of dynamic instability was computed using equation (7) and the results are plotted in Figures 8c and 8d. Comparing Figures 8a, 8c, and Figure 6, we can see that below 90 km, the large downward heat fluxes in winter and summer are associated with high probabilities in both convective and dynamic instabilities, while near 100 km the large downward heat flux in summer is primarily related to large dynamic instabilities.

[30] The total probability of instability, $P(Ri < 1/4) = P(N^2 < 0) + P(0 < Ri < 1/4)$, is plotted in Figures 8e and 8f. The annual mean probability is largest around 92 km at about 11% and decreases to less than 6% near 86 and 98 km. The contour plot of the total instability probability (Figure 9e) provides a better match with the heat flux (Figure 6) than either the convective or dynamic probability alone. Overall, larger downward heat fluxes correspond to higher $P(Ri < 1/4)$. This is clearly shown in Figure 10 where all the data are combined to derive a plot of the heat flux versus the average $P(Ri < 1/4)$. The overall averages of probabilities of dynamic, convective and total instabilities are marked in the figure along with the linear regression fit. The heat flux is signifi-

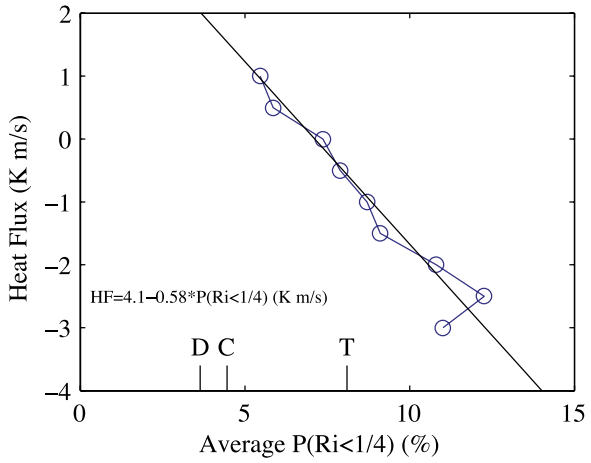

Figure 10. Heat flux versus averaged probability of total instability. For each heat flux value, the probability average is calculated using data within ±0.5 K m/s. The marks on the horizontal axis indicate the mean probabilities of dynamic (*D*), convective (*C*) and total (*T*) instabilities for all data points.

cantly different from zero only when the instability probability exceeds the overall average of about 8%.

[31] Above 93 km the heat flux is generally directed weakly upward ($\sim$ +0.5 K m s^{-1}) except during midsummer above 98 km where the heat flux is strongly downward (~ -2 K m s^{-1}). This large negative heat fluxes in summer have an uncertainty of ±0.34 K m s^{-1}, which suggests there is relatively strong downward heat transport in this region, most likely associated with large wind shears and enhanced probability of dynamic instability (see Figures 7c and 8c).

[32] Most of the positive heat flux measurements are less than about +0.5 K m s^{-1}, which is close to the average measurement uncertainty of ±0.34 K m s^{-1}. Above 98 km during the spring equinox period, the heat flux measurements are near +1 K m s^{-1}. In this case the value does exceed the measurement uncertainty, which suggests there is a weak, but statistically significant, upward heat transport in this region. Because wave activity in this region is exceptionally weak during the equinoxes and the instability probability is low (see Figures 4e, 5a, 7a, and 8e), this small upward heat transport must be associated with some other nongravity wave effect. While it is true that dissipating gravity waves generate negative heat fluxes, our measurements cannot differentiate between perturbations associated with gravity waves and with other effects. We measure the total wind and temperature perturbations from all sources. There are other mechanisms, such as transient wave decay or diabatic heating, that can induce upward heat flux [*Walterscheid*, 2001]. Exactly what mechanisms are responsible for this upward heat flux requires further investigation.

6. Zonal and Meridional Momentum Fluxes

[33] The vertical flux of horizontal momentum is a measure of the horizontal anisotropies of the wavefield. The momentum fluxes ($\overline{w'u'}$ and $\overline{w'v'}$) are defined as the expected value of the product of the vertical wind and zonal (u') and meridional (v') wind perturbations. The momentum flux vector points in the direction of greatest wave energy propagation for upward-propagating waves. If the wavefield is horizontally isotropic, or less restrictive, if the eastward (northward) momentum flux is equal to the westward (southward) flux, then the zonal (meridional) momentum flux is zero. The zonal and meridional momentum fluxes are shown in Figure 11. The zonal flux is mostly westward in winter months throughout the 85–100 m range. There is a peak eastward flux of over 4 m^2 s^{-2} in August at 91 km, and another peak of over 6 m^2 s^{-2} around May at 97 km. The meridional flux is mostly southward in winter throughout the entire region. In the spring through fall period, it is mostly northward below 92 km. Therefore the meridional flux exhibits a strong 12-month oscillation and is directed primarily toward the summertime pole. Above 92 km, the meridional flux is northward during the equinoxes but southward in summer, showing a dominant semiannual oscillation.

[34] The annual mean and 12- and 6-month amplitudes and phases of the momentum flux oscillations are tabulated for every 2.5 km between 85 and 100 km in Tables 3 and 4. The annual mean momentum fluxes are small compared to

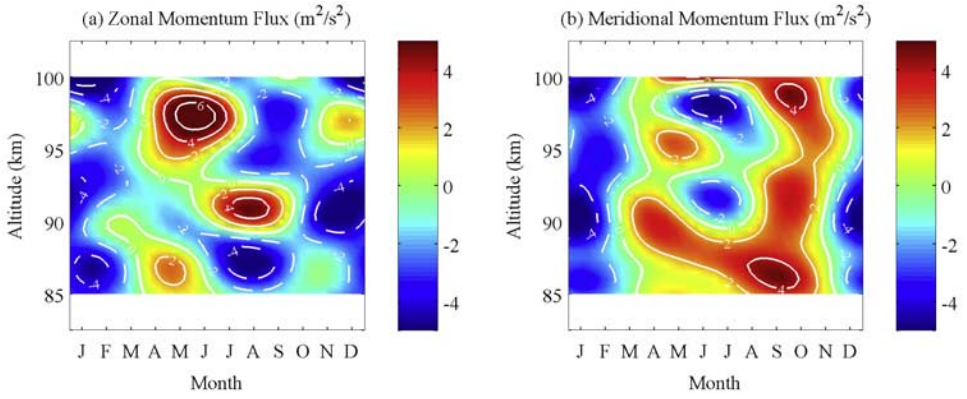

Figure 11. Seasonal variations of the measured vertical fluxes of (a) zonal momentum and (b) meridional momentum. The harmonic model uncertainties, which vary with altitude, average ±1.3 m^2 s^{-2} for the zonal flux and ±1.6 m^2 s^{-2} for the meridional flux and are tabulated in Tables 3 and 4.

Table 4. Measured Meridional Momentum Flux Parameters

Altitude, km	Annual Mean, $m^2\ s^{-2}$	12-Month Amplitude, $m^2\ s^{-2}$	12-Month Phase, month	6-Month Amplitude, $m^2\ s^{-2}$	6-Month Phase, month	Model Uncertainty, $m^2\ s^{-2}$
100.0	1.0 ± 0.78	3.6 ± 1.1	6.7 ± 0.6	1.5 ± 1.1	4.0 ± 0.7	±1.7
97.5	−1.0 ± 0.78	2.0 ± 1.1	10.3 ± 1.1	2.9 ± 1.1	3.3 ± 0.4	±1.7
95.0	−0.1 ± 0.76	1.2 ± 1.1	6.9 ± 1.8	2.5 ± 1.1	4.3 ± 0.4	±1.7
92.5	−0.5 ± 0.73	1.7 ± 1.0	8.3 ± 1.1	2.7 ± 1.0	3.2 ± 0.4	±1.6
90.0	−0.1 ± 0.70	2.4 ± 1.0	6.1 ± 0.8	3.4 ± 1.0	3.3 ± 0.3	±1.6
87.5	1.1 ± 0.61	3.0 ± 0.9	6.9 ± 0.6	0.8 ± 0.9	3.1 ± 1.1	±1.4
85.0	0.6 ± 0.53	2.2 ± 0.7	7.3 ± 0.6	1.4 ± 0.7	3.5 ± 0.5	±1.2

their seasonal variations throughout the mesopause region. The annual mean fluxes average less that about 1 $m^2\ s^{-2}$ depending on altitude, while the amplitudes of the 12- and 6-month oscillations can exceed 3 $m^2\ s^{-2}$ at some altitudes. When averaged throughout the 85- to 100-km height range, the annual mean zonal and meridional fluxes are $-1.2 \pm 0.22\ m^2\ s^{-2}$ and $+0.14 \pm 0.27\ m^2\ s^{-2}$, respectively. For comparison, the annual mean zonal and meridional wind velocities in this same height range are 11.3 m s^{-1} and −1.4 m s^{-1}, respectively. The net zonal wind between 85 and 100 km is eastward and the net zonal momentum flux is westward. The net meridional wind is weakly southward while the meridional flux is negligible.

[35] Radar measurements of momentum flux by *Tsuda et al.* [1990] showed weak meridional flux and a zonal flux that is westward in winter and eastward in summer. Our lidar measurements correspond to a higher altitude and therefore the fluxes are larger because of the increase in wave amplitude with altitude. Our meridional momentum flux peaks at about 4 $m^2\ s^{-2}$ compared with 1 $m^2\ s^{-2}$ in the measurements by *Tsuda et al.* [1990] and exhibits a clear seasonal variation in direction. Our lidar-measured zonal momentum flux is also slightly larger, 4 $m^2\ s^{-2}$ compared with 2 $m^2\ s^{-2}$ reported by *Tsuda et al.* [1990]. The most westward momentum flux in winter is consistent with their results but in summer, the lidar zonal momentum flux directions vary with altitude.

[36] The seasonal variation of the meridional flux below 90 km is also consistent with wave directions observed with an airglow imager at SOR [*Tang et al.*, 2002]. In the study of *Tang et al.* [2002], the momentum flux is generally northward in summer and southward in winter, the same as the directions from the lidar data at airglow altitude of about 87 km (Figure 11b). The magnitude of momentum flux in the study of Tang et al. is higher than what we derived here, mainly because the waves detected by airglow imagers are mostly higher-frequency waves which carry more momentum. The seasonal variations of momentum flux directions are believed to be associated with the seasonal change of meridional wind. When the in situ wind speed, in the direction of wave propagation, equals the intrinsic phase speed, critical layer effects will damp the wave [*Lindzen*, 1981; *Dunkerton and Fritts*, 1984]. Because critical layer filtering of waves by the mean winds has a significant influence on the horizontal distribution of wave propagation directions, the wavefield will be dominated by those waves that are propagating in a direction opposite to the winds at mesopause heights and below. The seasonal variation of the meridional momentum flux is therefore opposite to the variation of the meridional wind. This mean wind filtering effect is also evident in the seasonal variation of gravity wave directions observed by *Nakamura et al.* [1999] at Shigaraki, Japan (35°N, 136°E) and momentum flux by *Espy et al.* [2004a, 2004b] at Halley Station, Antarctica (75.6°S, 26.6°W).

[37] The distribution of the angle differences between the horizontal momentum flux and the mean horizontal wind vectors, computed every 0.5 km between 85- and 100-km altitude range for all the months, is illustrated in Figure 12. The distribution clearly shows that a dominant number of waves are propagating nearly opposite to the direction of the mean wind. In fact, for the SOR data set, the momentum flux vector is directed opposite the mean wind vector (angle difference between 90° and 270°) approximately two-thirds of the time.

7. Discussion and Conclusions

[38] The direct effect of heat transport by dissipating gravity waves is local heating or cooling. The heating rate due to heat flux convergence is

$$-\frac{1}{\bar{\rho}}\frac{\partial \bar{\rho}\langle w'T'\rangle}{\partial z} = -\frac{\partial \langle w'T'\rangle}{\partial z} + \langle w'T'\rangle\left(\frac{g}{R\bar{T}} + \frac{\mathrm{d}\ln \bar{T}}{\mathrm{d}z}\right). \quad (8)$$

The seasonal variation of heating rate, calculated from the heat flux data plotted in Figure 6, is shown in Figure 13. The heat flux has a strong downward component below 90 km in both summer and winter. The effect of this downward heat transport is strong cooling centered around

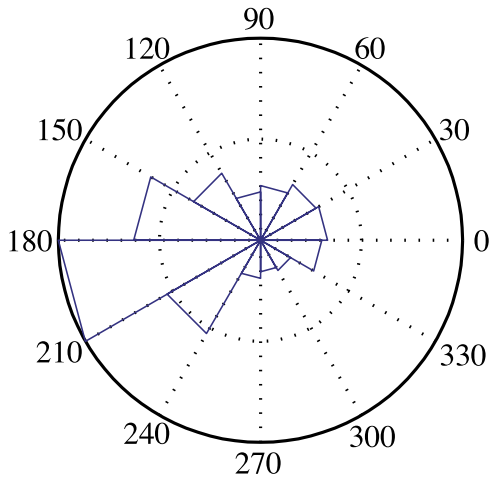

Figure 12. Distribution of angle differences between momentum flux and mean horizontal wind.

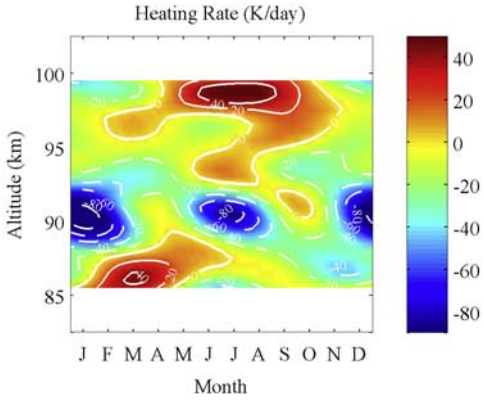

Figure 13. Heating rate due to heat flux convergence shown in Figure 6.

90 km. The cooling rate is larger than 80 K day^{-1} in summer and 100 K day^{-1} in winter. The annual mean cooling rate at this altitude exceeds 50 K day^{-1} (not shown). This dynamical cooling is likely balanced by chemical heating in this region [*Mlynczak and Solomon*, 1991, 1993; *Meriwether and Mlynczak*, 1995; *Chu et al.*, 2005].

[39] The most striking feature of the heat flux and heating rate is the strong 6-month oscillation. The heat flux is near zero around the equinoxes when the gravity wave activity is at minimum; on the other hand, the maximum downward flux occurs below 92 km near the solstices when the wind variances are at maximum. This strong 6-month oscillation may be related to the seasonal variation of tides. Semi-annual oscillations in the amplitude of the diurnal tide are predicted by general circulation models [*Vincent et al.*, 1988; *McLandress*, 2002] and have been observed [*Burrage et al.*, 1994, 1995; *McLandress et al.*, 1996]. Since the diurnal tide is stronger during the equinoxes and weaker during the solstices, our results suggest that critical layer filtering of waves by the strong diurnal tide at lower altitudes may be responsible for the weak gravity wave variances and heat flux in the mesopause region during the equinoxes.

[40] The accelerations of horizontal wind due to momentum flux convergence are shown in Figure 14. In the zonal direction, there is a maximum westward acceleration below 90 km in August and eastward above that exceeds 300 m s^{-1} day^{-1}. In the meridional direction, between 85 and 90 km, the strong upward flux of northward momentum from March to November (Figure 11b) generates a northward acceleration in excess of 200 m s^{-1} day^{-1}. These large values illustrate the significant impact of dissipating gravity waves on the mean circulation. Because the gravity waves also have large day-to-day variation, the momentum flux on individual nights can be even larger. For example, *Fritts et al.* [2002] observed a strong wave event at the MU Observatory in Japan that resulted in a mean wind acceleration of $\sim$ 80 m s^{-1} in less than an hour.

[41] In conclusion, the seasonal variations of fluxes appear to be linked to the seasonal variation of gravity wave activity in this region. The horizontal wind and temperature variances exhibit strong 6-month oscillations with maxima during the summer and winter solstices and minima during the spring and fall equinoxes. The vertical heat flux also exhibits large 6-month oscillations with maximum downward fluxes during winter and summer. The downward heat flux peaks near 88 km where the annual mean is -1.6 K m s^{-1}, but exceeds -3 K m s^{-1} at this altitude in mid-winter, and is nearly zero during the spring and fall equinoxes. The vertical structure and seasonal variations of the heat flux are closely related to the temperature lapse rate and vertical wind shear variances and to the probabilities of shear and convective instabilities. The heat flux is significant only when the instability probabilities exceed 8%, i.e., the mean value for the mesopause region at SOR. Comparisons between the heat flux and the probabilities of dynamic and convective instabilities suggest that below 90 km, the large downward heat flux in summer and winter is related to high probabilities in both dynamic and convective instabilities, while the large downward heat flux near 100 km in summer is mainly related to the high probability of dynamic instability.

[42] The momentum fluxes also exhibit strong seasonal variations. Although the annual mean meridional and zonal momentum fluxes are both less than about -1 m^2 s^{-2}, the 12- and 6-month amplitudes can exceed 3 m^2 s^{-2} at certain altitudes. Below 90 km, the meridional momentum flux is northward during the summer and southward during the winter, exactly opposite to the mean meridional wind. Two-

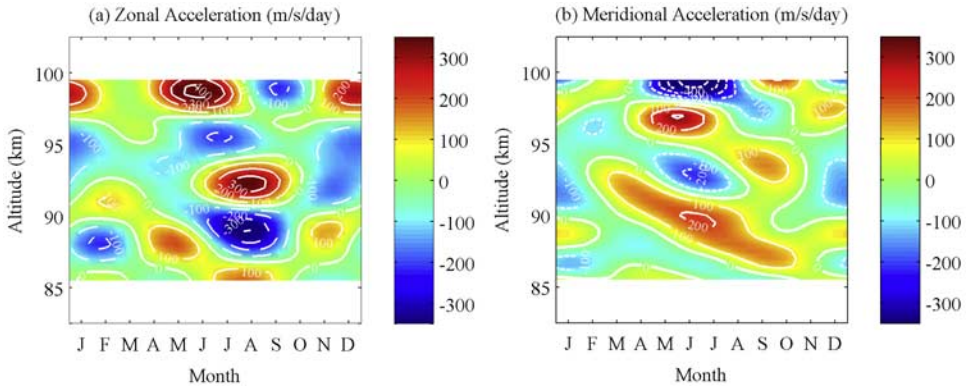

Figure 14. (a) Zonal and (b) meridional accelerations of horizontal wind due to vertical fluxes of horizontal momentum.

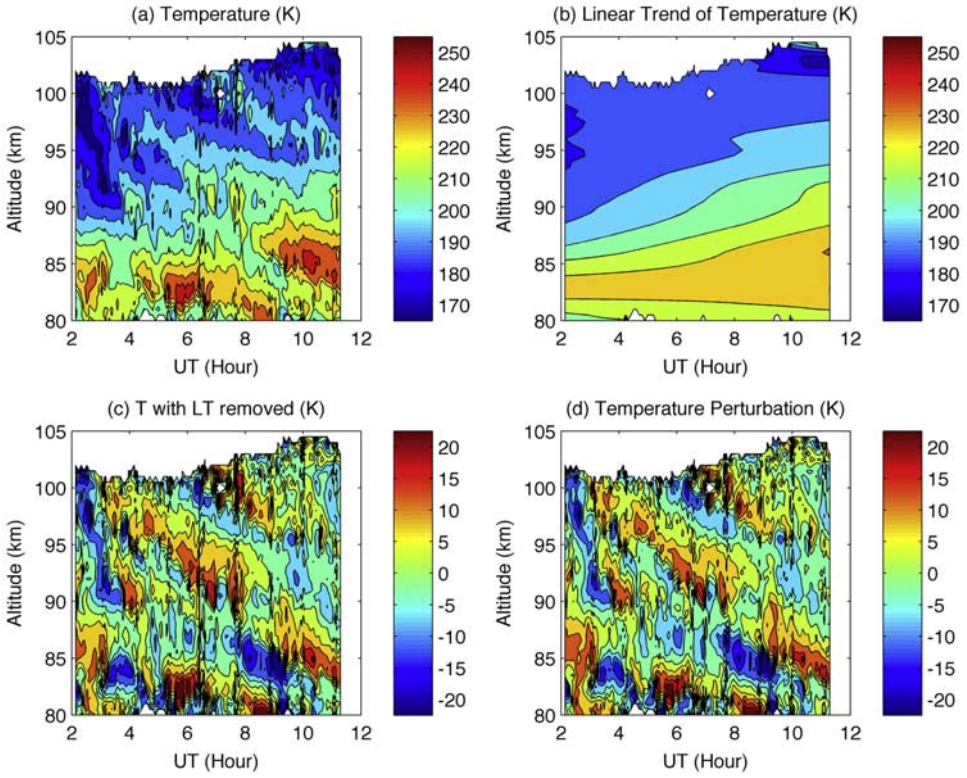

Figure 15. Illustration of data processing for temperature on 5 January 2000: (a) temperature measured at zenith; (b) linear trend of temperature in time; (c) temperature perturbations after removing the linear trend in time; and (d) temperature perturbations after removing the linear trend in time and the vertical mean.

thirds of the time the horizontal momentum flux is directed against the mean wind field.

Appendix A: Deriving Wind and Temperature Variances and Momentum and Heat Fluxes From the Wind and Temperature Data

[43] The first step is to derive wave perturbations. First, data points with photon noise errors larger than 10 m s^{-1} or 10 K were discarded. To eliminate potential biases associated with gravity waves whose periods exceed the observation period, for each night of observations and each off-zenith pointing direction, the instantaneous LOS wind and temperature perturbations were computed by subtracting the linear trend in time at each altitude in the profile. Perturbations that exceeded three standard deviations from the nightly mean were discarded to remove occasional outliers. This linear fitting and quality control procedures were then repeated on the reduced data set. This iterative procedure eliminates outliers and perturbations associated with gravity waves whose periods are longer than about twice the observation period. The outliers removed constitute small portion of the entire data set (< 1% between 85 and 100 km). Finally, the vertical mean was subtracted from each perturbation profile to eliminate the effects of waves whose vertical wavelengths are longer than about twice the profile height range ($\sim$ 30 km). This process is done separately for each of the five beam directions. As an example, the data processing for the night on 5 January 2000 is shown in Figures 15 and 16. Figure 15 shows the temperature measured at zenith. On this night, the temperature has strong wave perturbations (Figure 15a). In Figure 15b, the linear trend in time shows that the background temperature decreases with altitude from 82 km up and increases gradually at each altitude through the night. After this linear trend in time is removed, the wave perturbations are more pronounced as shown in Figure 15c. Figure 15d shows the final temperature perturbation, after the vertical mean in Figure 15c is removed. The difference between Figures 15c and 15d is small. Figure 16a shows the vertical wind at 92 km along with its linear trend. The linear trend shows a decrease of vertical wind over the night, with the increase of temperature in Figure 16c. The residual vertical wind, after the linear trend and vertical mean are removed, is shown in Figure 16b. The effect of the removal of the vertical average is small. The vertical wind perturbation is several m s^{-1} significant compared with its photon noise error ($\sim$ 1 m s^{-1}). Even though the limited observation period and altitude coverage make it difficult to completely remove the effects of long period and large vertical scale waves, the above example shows that the linear trend and vertical mean removal is effective in obtaining the appropriate perturbations. It is well known that the temperature spectrum varies approximately as ω^{-2} while the vertical wind spectrum varies approximately as ω^{0}, where ω is the temporal frequency. Consequently, temperature perturbations are dominated by low-frequency fluctuations while the vertical wind perturbations are rich

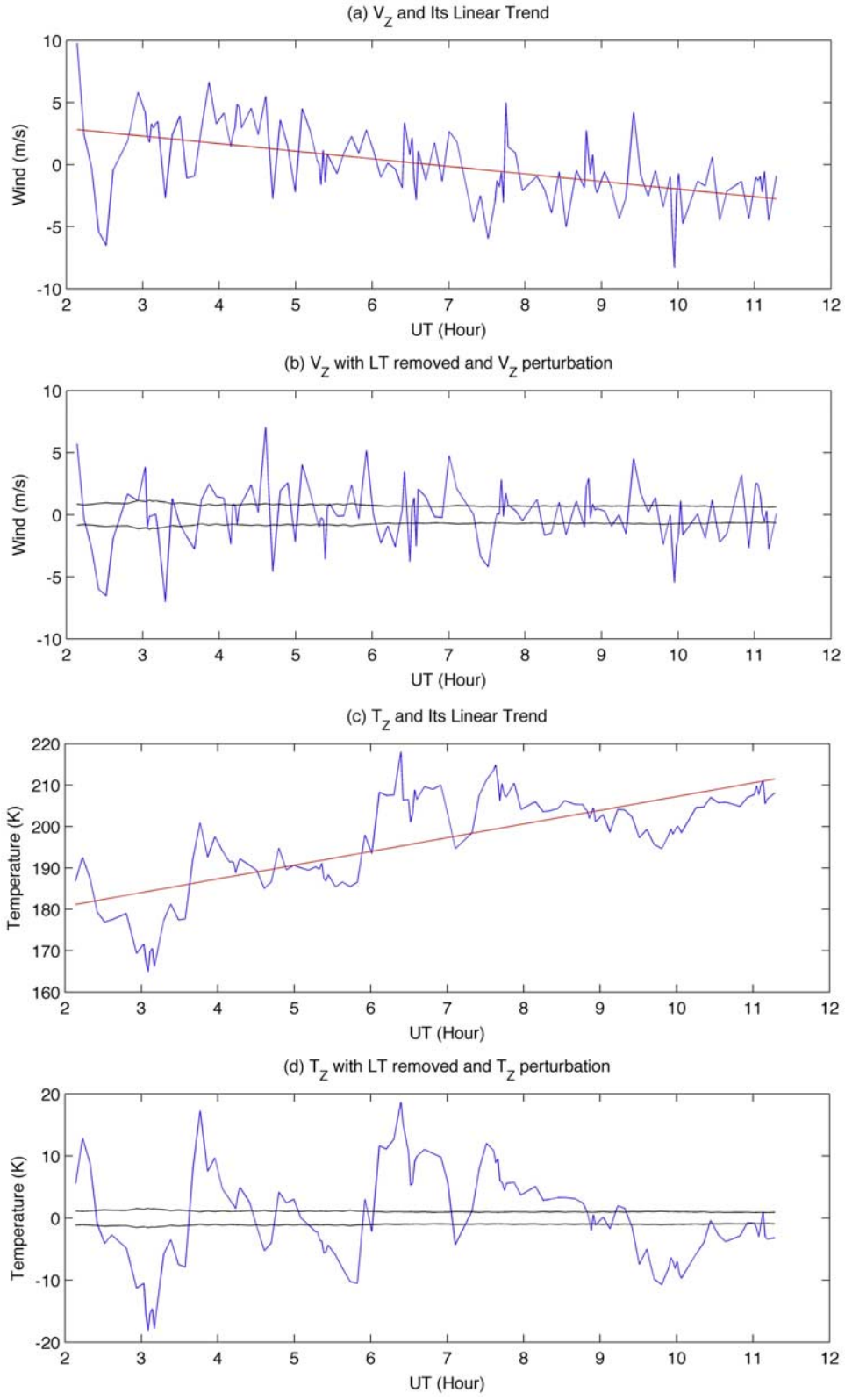

Figure 16. Illustration of data processing for vertical wind and temperature at 92 km on 5 January 2000: (a) vertical wind (blue) and its linear trend (red); (b) vertical wind perturbation (blue) and errors of vertical wind due to photon noise (black lines); (c) and (d) are similar except for temperature.

in all frequencies. The perturbations plotted in Figure 16d exhibit these characteristics.

[44] The temperature variance for each month was calculated by averaging the squares of temperature perturbation from all profiles within that month. For the wind, we need to consider their relations with the LOS wind. The vertical (w), zonal (u), and meridional (v) components of the wind are related to the measured LOS wind profiles as follows,

$$\begin{aligned} V_Z &= w \\ V_E &= u\,\sin\theta + w\,\cos\theta \\ V_W &= -u\,\sin\theta + w\,\cos\theta \\ V_N &= v\,\sin\theta + w\,\cos\theta \\ V_S &= -v\,\sin\theta + w\,\cos\theta \end{aligned} \tag{A1}$$

where V_Z, V_E, V_W, V_N, and V_S are LOS winds measured at the zenith, east, west, north, and south positions, respectively, and θ is the zenith angle, equal to 10°. The vertical wind variance was calculated in the same way as temperature from all zenith wind measurements. The variances of the horizontal wind perturbation were calculated as

$$\begin{aligned} \overline{u'u'} &= \frac{\overline{V_E'^2} + \overline{V_W'^2} - 2\overline{V_Z'^2}\,\sin^2\theta}{2\,\sin^2\theta}, \\ \overline{v'v'} &= \frac{\overline{V_N'^2} + \overline{V_S'^2} - 2\overline{V_Z'^2}\,\sin^2\theta}{2\,\sin^2\theta}, \end{aligned} \tag{A2}$$

where the prime represents the perturbation and the overbar denotes sample averaging. The perturbation variance for each pointing direction, $\overline{V_E'^2}$, $\overline{V_W'^2}$, $\overline{V_N'^2}$, $\overline{V_S'^2}$, $\overline{V_Z'^2}$ was estimated by averaging the squares of all perturbation profiles collected in that direction during the month.

[45] Profiles of the vertical fluxes of zonal ($\overline{w'u'}$) and meridional ($\overline{w'v'}$) momentum were computed using the dual-beam, off-zenith radial wind data following the approach of *Vincent and Reid* [1983]. The assumption with this method is that the second-order statistics is homogeneous within the volume covered by the dual beam. The small horizontal separation of the lidar beams, about 30 km at 90-km altitude, assures that this assumption is valid. The zonal (meridional) flux profiles were then derived by differencing the monthly mean perturbation variances computed using the east (north) and west (south) beam data as

$$\begin{aligned} \overline{w'u'} &= \frac{\overline{V_E'^2} - \overline{V_W'^2}}{4\,\sin\theta\,\cos\theta}, \\ \overline{w'v'} &= \frac{\overline{V_N'^2} - \overline{V_S'^2}}{4\,\sin\theta\,\cos\theta}. \end{aligned} \tag{A3}$$

By computing the momentum fluxes this way, each 90-s LOS wind profile contributes equally to the monthly mean flux profile. The momentum flux profiles were then smoothed vertically using a Hamming window of 2.5-km full-width at half-maximum (FWHM). The monthly average flux profiles derived using this data processing method have a vertical resolution of 2.5 km and include the effects of all gravity waves with vertical wavelengths greater than 1 km and less than about 30 km and periods greater than 3 min and less than about 14 hours, which is twice the average observation period of 7 hours.

[46] The uncertainties in the momentum flux measurements were computed using the formulas derived by *Thorsen et al.* [2000] for the special case where the LOS wind perturbations measured by the two coplanar beams are uncorrelated:

$$\begin{aligned} \mathrm{Var}\left(\overline{w'u'}\right) &\approx \frac{\Delta z_{\mathrm{MF}}}{nL}\left[\frac{\mathrm{Var}(w')\mathrm{Var}(u')}{2} + \frac{\mathrm{Var}^2(w')}{4\tan^2\theta} + \mathrm{Var}^2(u')\tan^2\theta\right] \\ \mathrm{Var}\left(\overline{w'v'}\right) &\approx \frac{\Delta z_{\mathrm{MF}}}{nL}\left[\frac{\mathrm{Var}(w')\mathrm{Var}(v')}{2} + \frac{\mathrm{Var}^2(w')}{4\tan^2\theta} + \mathrm{Var}^2(v')\tan^2\theta\right] \end{aligned} \tag{A4}$$

where Δz_{MF} is the measured vertical correlation length of the momentum flux, equal to 1 km; L is the averaging altitude range, equal to 2.5 km; and n is the total number of radial wind profiles used to compute the mean momentum flux profile [*Gardner and Yang*, 1998]. This worst-case formula applies to our measurement scenario because the minimum time between any two coplanar beam measurements ($\sim$ 6 min) is comparable to the flux correlation time ($\Delta t_{\mathrm{HF}} \approx 10$ min) and so they are uncorrelated.

[47] The vertical heat flux ($\overline{w'T'}$) profiles were computed using the vertical wind and temperature perturbation profiles derived from the zenith-pointing beam [*Gardner and Yang*, 1998; *Liu and Gardner*, 2004, 2005]. Like the momentum fluxes, all the heat flux profiles measured during a given month were averaged and then smoothed vertically using a Hamming window of 2.5 km FWHM. The monthly average heat flux profiles have a vertical resolution of 2.5 km and include the effects of all gravity waves with vertical wavelengths greater than 1 km and less than about 30 km and periods greater than 3 min and less than about 14 hours. The heat flux error is given approximately by

$$\mathrm{Var}\left(\overline{w'T'}\right) \approx \frac{\Delta z_{\mathrm{HF}}}{nL}\mathrm{Var}(w')\mathrm{Var}(T') \tag{A5}$$

where Δz_{HF} is the vertical correlation lengths for the heat and dynamical fluxes, equal to 1 km; L is the averaging altitude range, equal to 2.5 km; and n is the number of flux profiles used to compute the means [*Gardner and Yang*, 1998; *Liu and Gardner*, 2004, 2005]. This formula applies to our measurement scenario because the minimum time between two zenith beam measurements ($\sim$ 6 min) is comparable to the flux correlation times ($\Delta t_{\mathrm{HF}} \approx 10$ min) and so the instantaneous flux profiles are uncorrelated.

[48] The accuracy of the wind measurements can affect the accuracies of the estimated heat and momentum fluxes. The absolute wind measurement accuracy of this Na lidar has been thoroughly validated through several studies that compared the lidar measurements with winds derived from meteor trail advection measurements [*Grime et al.*, 2000], trimethylaluminum (TMA) trails released by a rocket launched from White Sands Missile Range [*Larsen et al.*, 2003], and meteor radar measurements [*Liu et al.*, 2002; *Franke et al.*, 2005]. These studies found that the absolute LOS wind error, which is limited by knowledge of the absolute frequency or wavelength of the laser, is no larger than the photon noise error (at most ~ 1 m s^{-1}). An error in the assumed laser frequency will introduce a fixed bias in the radial winds measured at each altitude in a profile. The

lidar frequency is calibrated by assuming that the mean vertical wind between 85 and 100 km is zero. The data are processed by continuously adjusting the laser frequency so that mean vertical wind is zero. Since the most sophisticate atmospheric models predict that vertical upwelling and downwelling velocities are at most a few cm s^{-1} in this region, the LOS wind errors are dominated by photon noise, not calibration errors.

[49] Furthermore, all the flux measurements depend on wind perturbations, not absolute winds. Any residual wind bias, associated with a small error in the assumed laser frequency, is removed when the wind perturbations are computed (that is, bias is removed when the vertical mean LOS wind is subtracted to compute the wind perturbations). At 500-m resolution and 90-s integration period, the variance of the random LOS and vertical wind error associated with photon noise is about 1 m^2 s^{-2} between 85 and 100 km for each profile measured. This error is quickly reduced to negligible levels when the data are subsequently averaged over tens of hours to make the flux calculations. The dominant error source in the flux calculation is the geophysical variation (i.e., variance) in the vertical wind, horizontal wind, and temperature (see (A4) and (A5)).

[50] **Acknowledgments.** The authors gratefully acknowledge the support by Robert Fugate, Director of the Starfire Optical Range, and his staff. The authors thank Xinzhao Chu and Peter Dragic for their help operating the Na wind/temperature lidar at SOR. This work was supported by NSF ATM-00-03198 and ATM-03-38425.

References

Alexander, M. J., and J. R. Holton (1997), A model study of zonal forcing in the equatorial stratosphere by convectively induced gravity waves, *J. Atmos. Sci.*, *54*, 408–419.

Burrage, M. D., D. N. Arvin, W. R. Skinner, and P. B. Hays (1994), Observations of the O_2 atmospheric band nightglow by the high resolution Doppler imager, *J. Geophys. Res.*, *99*, 15,017–15,024.

Burrage, M. D., M. E. Hagan, W. R. Skinner, D. L. Wu, and P. B. Hays (1995), Long-term variability in the solar diurnal tide observed by HRDI and simulated by the GSWM, *Geophys. Res. Lett.*, *22*, 2641–2644.

Chu, X., C. S. Gardner, and S. J. Franke (2005), Nocturnal thermal structure of the mesosphere and lower thermosphere region at Maui, Hawaii (20.7°N), and Starfire Optical Range, New Mexico (35°N), *J. Geophys. Res.*, *110*, D09S03, doi:10.1029/2004JD004891.

Dunkerton, T. J., and D. C. Fritts (1984), Transient gravity-wave critical layer interaction: 1. Convective adjustment and the mean zonal acceleration, *J. Atmos. Sci.*, *41*, 992–1007.

Espy, P. J., G. O. L. Jones, G. R. Swenson, J. Tang, and M. J. Taylor (2004a), Seasonal variations of the gravity wave momentum flux in the Antarctic mesosphere and lower thermosphere, *J. Geophys. Res.*, *109*, D23109, doi:10.1029/2003JD004446.

Espy, P. J., G. O. L. Jones, G. R. Swenson, J. Tang, and M. J. Taylor (2004b), Tidal modulation of the gravity wave momentum flux in the Antarctic mesosphere, *Geophys. Res. Lett.*, *31*, L11111, doi:10.1029/2004GL019624.

Franke, S. J., X. Chu, A. Z. Liu, and W. K. Hocking (2005), Comparison of meteor radar and Na Doppler lidar measurements of winds in the mesopause region above Maui, Hawaii, *J. Geophys. Res.*, *110*, D09S02, doi:10.1029/2003JD004486.

Fritts, D. C., and M. J. Alexander (2003), Gravity wave dynamics and effects in the middle atmosphere, *Rev. Geophys.*, *41*(1), 1003, doi:10.1029/2001RG000106.

Fritts, D. C., and Z. G. Luo (1995), Dynamical and radiative forcing of the summer mesopause circulation and thermal structure: 1. Mean solstice conditions, *J. Geophys. Res.*, *100*, 3119–3128.

Fritts, D. C., and P. K. Rastogi (1985), Convective and dynamic instabilities due to gravity wave motions in the lower and middle atmosphere: Theory and observations, *Radio Sci.*, *20*, 1247–1277.

Fritts, D. C., S. L. Vadas, and Y. Yamada (2002), An estimate of strong local body forcing and gravity wave radiation based on OH airglow and meteor radar observations, *Geophys. Res. Lett.*, *29*(10), 1429, doi:10.1029/2001GL013753.

Garcia, R. R., and S. Solomon (1985), The effect of breaking gravity waves on the dynamics and chemical composition of the mesosphere and lower thermosphere, *J. Geophys. Res.*, *90*, 3850–3868.

Gardner, C. S. (1994), Diffusive filtering theory of gravity wave spectra in the atmosphere, *J. Geophys. Res.*, *99*, 20,601–620,622.

Gardner, C. S., and W. Yang (1998), Measurements of the dynamical cooling rate associated with the vertical transport of heat by dissipating gravity waves in the mesopause region at the Starfire Optical Range, New Mexico, *J. Geophys. Res.*, *103*, 16,909–916,926.

Gardner, C. S., Y. Zhao, and A. Z. Liu (2002), Atmospheric stability and gravity wave dissipation in the mesopause region, *J. Atmos. Sol. Terr. Phys.*, *64*, 923–929, doi:10.1016/S1364-6826(1002)00047-00040.

Grime, B. W., T. J. Kane, A. Z. Liu, G. C. Papen, C. S. Gardner, M. C. Kelley, C. Kruschwitz, and J. Drummond (2000), Meteor trail advection observed during the 1998 Leonid shower, *Geophys. Res. Lett.*, *27*, 1819.

Hamilton, K. (1996), Comprehensive meteorological modeling of the middle atmosphere: A tutorial review, *J. Atmos. Sol. Terr. Phys.*, *58*, 1591–1627.

Hines, C. O. (1970), Eddy diffusion coefficients due to instabilities in internal gravity waves, *J. Geophys. Res.*, *75*, 3937–3939.

Hodges, R. R. (1967), Generation of turbulence in the upper atmosphere by internal gravity waves, *J. Geophys. Res.*, *72*, 3455–3458.

Hodges, R. R. (1969), Eddy diffusion coefficients due to instabilities in internal gravity waves, *J. Geophys. Res.*, *74*, 4087–4090.

Holton, J. R. (1983), The influence of gravity wave breaking on the circulation of the middle atmosphere, *J. Atmos. Sci.*, *40*, 2497–2507.

Kudeki, E., and S. J. Franke (1998), Statistics of momentum flux estimation, *J. Atmos. Sol. Terr. Phys.*, *60*, 1549–1553.

Larsen, M. F., A. Z. Liu, R. L. Bishop, and J. H. Hecht (2003), TOMEX: A comparison of lidar and sounding rocket chemical tracer wind measurement, *Geophys. Res. Lett.*, *39*(7), 1375, doi:10.1029/2002GL015678.

Lindzen, R. S. (1981), Turbulence and stress owing to gravity wave and tidal breakdown, *J. Geophys. Res.*, *86*, 9707–9714.

Liu, A. Z., and C. S. Gardner (2004), Vertical dynamical transport of mesospheric constituents by dissipating gravity waves, *J. Atmos. Sol. Terr. Phys.*, *66*(3-4), 267–275, doi:10.1016/j.jastp.2003.1011.1002.

Liu, A. Z., and C. S. Gardner (2005), Vertical heat and constituent transport in the mesopause region by dissipating gravity waves at Maui, Hawaii (20.7°N), and Starfire Optical Range, New Mexico (35°N), *J. Geophys. Res.*, *110*, D09S13, doi:10.1029/2004JD004965.

Liu, A. Z., W. K. Hocking, S. J. Franke, and T. Thayaparan (2002), Comparison of Na lidar and meteor radar wind measurements at Starfire Optical Range, NM, USA, *J. Atmos. Sol. Terr. Phys.*, *64*, 31–40.

Luo, Z., D. C. Fritts, R. W. Portmann, and G. E. Thomas (1995), Dynamical and radiative forcing of the summer mesopause circulation and thermal structure: 2. Seasonal-variations, *J. Geophys. Res.*, *100*, 3129–3137.

Matsuno, T. (1982), A quasi one-dimensional model of the middle atmosphere circulation interacting with internal gravity waves, *J. Meteorol. Soc. Japan*, *60*, 215–226.

McLandress, C. (2002), The Seasonal variation of the propagating diurnal tide in the mesosphere and lower thermosphere. part I: The role of gravity waves and planetary waves, *J. Atmos. Sci.*, *59*, 893–906.

McLandress, C., G. G. Shepherd, and B. H. Solheim (1996), Satellite observations of thermospheric tides: Results from the Wind Imaging Interferometer on UARS, *J. Geophys. Res.*, *101*, 4093–4114.

Meek, C. E., I. M. Reid, and A. H. Manson (1985), Observations of mesospheric wind velocities: 2. Cross sections of power spectral density for 48–8 h, 8–1 h, 1h–10 min over 60–110 km for 1981, *Radio Sci.*, *20*, 1383–1402.

Meriwether, J. W., and M. G. Mlynczak (1995), Is chemical heating a major cause of the mesospheric inversion layer?, *J. Geophys. Res.*, *100*, 1379–1387.

Mlynczak, M. G., and S. Soloman (1991), Middle atmosphere heating by exothermic chemical reactions involving odd-hydrogen species, *Geophys. Res. Lett.*, *18*, 37–40.

Mlynczak, M. G., and S. Soloman (1993), A detailed evaluation of the heating efficiency in the middle atmosphere, *J. Geophys. Res.*, *98*, 10,517–10,541.

Nakamura, T., A. Higashikawa, T. Tsuda, and Y. Matsushita (1999), Seasonal variations of gravity wave structures in OH airglow with a CCD imager at Shigaraki, *Earth Planets Space*, *51*, 897–906.

Tang, J., A. Z. Liu, and G. R. Swenson (2002), High frequency gravity waves observed in OH airglow at Starfire Optical Range, NM: Seasonal variations in momentum flux, *Geophys. Res. Lett.*, *29*(20), 1966, doi:10.1029/2002GL015794.

Thorsen, D., S. J. Franke, and E. Kudeki (2000), Statistics of momentum flux estimation using the dual coplanar beam technique, *Geophys. Res. Lett.*, *27*, 3193–3196.

Tsuda, T., Y. Murayama, M. Yamamoto, S. Kato, and S. Fukao (1990), Seasonal variation of momentum flux in the mesosphere observed with the MU radar, *Geophys. Res. Lett.*, *17*, 725–728.

Walterscheid, R. L. (1981), Dynamical cooling induced by dissipating internal gravity waves, *Geophys. Res. Lett.*, *8*, 1235–1238.

Walterscheid, R. L. (2001), Gravity wave transports and their effects on the large-scale circulation of the upper mesosphere and lower thermosphere, *Adv. Space Res.*, *27*, 1713–1721.

Weinstock, J. (1983), Heat flux induced by gravity waves, *Geophys. Res. Lett.*, *10*, 165–167.

Vincent, R. A., and D. C. Fritts (1987), A climatology of gravity wave motions in the mesopause region at Adelaide, Australia, *J. Atmos. Sci.*, *44*, 748–760.

Vincent, R. A., and I. M. Reid (1983), HF Doppler measurements of mesospheric gravity wave momentum fluxes, *J. Atmos. Sci.*, *40*, 1321–1333.

Vincent, R. A., T. Tsuda, and S. Kato (1988), A comparative study of mesospheric solar tides observed at Adelaide and Kyoto, *J. Geophys. Res.*, *93*, 699–708.

Zhao, Y., A. Z. Liu, and C. S. Gardner (2003), Measurements of atmospheric stability in the mesopause region at Starfire Optical Range, NM, *J. Atmos. Sol. Terr. Phys.*, *65*, 219–232.

C. S. Gardner and A. Z. Liu, Department of Electrical and Computer Engineering, University of Illinois, 308 CSRL, 1308 West Main Street Urbana, IL 61801, USA. (liuzr@uiuc.edu)